



R3 Revealed – Inside Views from Calcined Clay Calorimetry Brews

Pengfei Zhao and Karl Peterson^(✉)

University of Toronto, 35 St. George Street, Toronto, ON M5S 1A4, Canada
pf.zhao@mail.utoronto.ca, karl.peterson@utoronto.ca

Abstract. The R3 test method is currently experiencing rapid adoption worldwide as an essential tool for the assessment of potential supplementary cementitious materials for use in concrete. Originally developed for calcined clays, the resultant hydration phase assemblages have been well characterized by bulk techniques such as X-ray diffraction, thermogravimetric analysis, and nuclear magnetic resonance, but relatively less work has been dedicated to seeing, microscopically, the inner workings of the method. With this in mind, this foray into the formerly private world of calcined clay pastes was undertaken, to see what goes on behind those closed calorimeter chamber doors. Like some sort of scientific construction materials conference proceedings click-bait, this abstract is intended to whet the appetite of those who demand to know more about such elusive and camera-shy phases as monocarbonate and katoite. And for those who choose to turn the page, and succumb to such temptations: buckle your seatbelts for a twisted tortuous ride through hydrated paste pore structure, as revealed by fluorescent epoxy impregnation and scanning electron microscope images.

Keywords: Calcined Clays · Isothermal Calorimetry · Scanning Electron Microscope

1 Introduction

Limestone calcined clay cement (LC3) is widely recognized as a successful innovation in the realm of sustainable building materials. LC3 cement has demonstrated the potential to substitute 45% of Portland cement with 30% calcined clays and 15% limestone, while maintaining a similar strength and durability in concrete [1–3]. The clays with a kaolinite content of at least 40% are considered suitable for LC3 cement production [4], while limestone is used not only as a filler but also as a reactive component. Limestone has been shown to react with alumina from metakaolin in the presence of calcium hydroxide, resulting in the formation of monocarbonate and the stabilization of ettringite [5, 6]; both are beneficial for the strength and durability of cementitious materials.

The reactivity of calcined clays used in LC3 cement can be determined using the R3 test method [7]. The R3 test method measures the cumulative heat release or bound water content in a hydrated paste that is cured at 40 °C for 7 days. The paste, which is designed to simulate the environment in LC3 cement, consists of a mixture of the

calcined clay, calcium hydroxide, calcium carbonate, potassium hydroxide, potassium sulfate, and de-ionized water. Although the R3 test method was originally developed to provide a rapid and accurate evaluation for the reactivity of calcined clays, it has recently been adopted as ASTM C1897 [8] and is now used to determine the reactivity of a wide range of supplementary cementitious materials (SCMs) including slags and fly ashes [9].

While kaolinite is generally considered to be superior to other clay minerals in terms of pozzolanic reactivity when calcined, there is growing interest in other clay minerals such as montmorillonite and illite as potential sources of SCMs [10–13]. However, the possibility of using these clay minerals in LC3 cement, and the effect of limestone on their hydration process, have not been extensively studied. Further research is therefore necessary to understand their performance in LC3 cement. In addition to commonly used phase characterization techniques, such as X-ray diffraction (XRD) and thermogravimetric analysis (TGA), this project also focuses on the microscopic analysis to provide more detailed insights into the microstructure and properties of hydrated R3 mixes containing these calcined clays.

2 Experimental

2.1 Materials

Standard clay minerals of kaolinite, montmorillonite, and illite were studied in this project. The chemical composition of three clay minerals was characterized using X-ray fluorescence (XRF), and the results are listed in Table 1. For thermal activation, each clay was calcined at a specific temperature: kaolinite at 600 °C, montmorillonite at 800 °C, and illite at 900 °C. The calcination process was carried out in a temperature controlled Thermo Scientific furnace and lasted for 2 h. These specific temperatures were chosen based on the reactivity of each clay sample when calcined over a range of temperatures (i.e., 600, 700, 800, 900, and 1000 °C), and are consistent with the optimal activation temperatures reported in the literature for the three clay minerals [10–12, 14].

2.2 Calorimetry

The isothermal calorimetry was performed for the three calcined clays according to ASTM C1897 [8], using a Calmetrix I-Cal 8000 HPC isothermal calorimeter. To understand the effect of limestone on the hydration of different calcined clays, the same standardized procedures were followed for calorimetry of the three calcined clays, except that calcite was not added to the mix. The cumulative heat per gram of SCM for each sample was calculated as the average value of two parallel tests. After completing the calorimetry tests, hydration in the pastes was immediately stopped by solvent exchange with isopropanol for two days followed by one day vacuum drying with silica gel and soda lime.

Table 1. Chemical composition of three clay mineral samples.

| % weight | kaolinite | montmorillonite | illite |
|---------------------------------|-----------|-----------------|--------|
| LOI at 1000 °C | 14.10 | 16.27 | 5.76 |
| SiO ₂ | 44.93 | 51.59 | 61.10 |
| Al ₂ O ₃ | 39.05 | 18.28 | 18.07 |
| Fe ₂ O ₃ | 0.33 | 5.05 | 4.47 |
| CaO | 0.02 | 2.03 | 0.86 |
| MgO | 0.18 | 3.30 | 2.39 |
| SO ₃ | - | 0.06 | 0.03 |
| K ₂ O | 0.09 | 0.55 | 6.09 |
| Na ₂ O | 0.03 | 2.07 | 0.22 |
| TiO ₂ | 1.45 | 0.14 | 0.83 |
| P ₂ O ₅ | 0.06 | 0.07 | 0.12 |
| Mn ₂ O ₃ | - | 0.04 | 0.04 |
| SrO | - | 0.02 | - |
| ZnO | - | 0.01 | 0.01 |
| Sum | 100.25 | 100.01 | 100.26 |
| Na ₂ O _{eq} | 0.09 | 2.43 | 4.23 |

2.3 XRD and TGA

The dried pastes were characterized by XRD and TGA. The XRD patterns were recorded on a Philips PW 3040/60 X-ray diffractometer, operating at 40 kV and 30 mA with a Cu-K α radiation source. The 2-theta scanning range was set between 5° and 70°, with a step size of 0.017° and a counting time of 20 s. TGA was performed using a Netzsch STA 409 instrument with a constant heating rate of 10 °C/min from ambient to 1000 °C under a stable nitrogen gas flux of approximately 100 ml/min.

2.4 Microscopy

Fragments of the paste were placed in an open 50 ml polypropylene centrifuge tube, and the empty spaces between the fragments filled with 0.6–0.8 mm diameter (20–30 mesh) silica sand. The tube was placed under vacuum, filled with fluorescent dyed epoxy, brought back to atmospheric pressure, and the epoxy allowed to harden. The tube was cut lengthwise to expose the fragments, trimmed to billet size, and a flat surface ground using a kerosene-cooled 64 μ m grit diamond wheel. The billets were placed face down in a tray, placed under vacuum, and fluorescent epoxy added to the tray, enough to immerse the ground surfaces in epoxy. After returning to atmospheric pressure, the billets were removed from the tray, with the ground surfaces pressed flat against a low density polyethylene plastic sheet, and the epoxy allowed to harden. The veneer of

fluorescent epoxy was removed from the ground surface, and the billets prepared in 60 μm thick polished thin sections—twice as thick as standard 30 μm thin sections. The extra thickness was employed due to concerns around excessive thinning that might occur during final polishing, given the soft nature of the paste fragments. The thin sections were imaged with an Olympus BX-60 petrographic fluorescence microscope. Finally, the thin sections were carbon coated, and examined with a JEOL JSM6610-Lv scanning electron microscope (SEM) equipped with an Oxford X-ray energy dispersive spectroscopy (EDS) silicon drift detector (SDD). Both back-scattered electron (BSE) and characteristic $K\alpha$ X-ray elemental images were collected.

3 Results and Discussion

3.1 Calorimetry

Figure 1 demonstrates the effect of calcite on the cumulative heat release for the three calcined clays. For kaolinite at 600 °C (metakaolin), the cumulative heat release in the paste with calcite increased faster than that in the paste without calcite, particularly in the first two days, indicating a beneficial influence of calcite on the early-age hydration of metakaolin. However, the difference in cumulative heat between the two pastes became less pronounced about three days later. At 7 days, the average cumulative heat for the paste with and without calcite was 882.0 and 833.6 J/g of SCM, respectively. In comparison, the addition of calcite had a limited effect on the evolution of cumulative heat release for montmorillonite at 800 °C and illite at 900 °C.

3.2 XRD and TGA

Figure 2 displays the XRD patterns for the hydrated pastes containing the three calcined clays, with and without the addition of calcite. In the case of kaolinite 600 °C pastes, due to the chemical reaction between alumina from metakaolin, carbonate from calcite, and calcium from both portlandite and calcite [5], monocarbonate ($\text{C}_4\text{A}\bar{\text{C}}\text{H}_{11}$) is the major crystalline phase detected in its hydrated R3 mix, as expected. However, if calcite is not included in the paste, katoite (C_3AH_6) is formed instead [15]. For montmorillonite 800 °C and illite 900 °C pastes, the XRD patterns were found to be similar regardless of the presence of calcite. In both cases, the primary crystalline phase observed is a hydrotalcite-like phase (M_4AH_{10}), where magnesium is derived from the thermal decomposition of the respective clay minerals. However, it is worth mentioning that no C-S-H or C-A-S-H phases were found in XRD patterns, as they are likely to be poorly crystallized and do not exhibit strong XRD reflections.

Figure 3 presents the derivative thermogravimetry (DTG) results for the hydrated pastes with and without calcite. Typically, peaks that occur in the temperature range of 80 and 240 °C are associated with the dehydration of C-S-H phases [16]. Within this temperature range, the metakaolin paste with calcite exhibits a more significant water loss compared to the paste without calcite. However, this water loss could be also contributed by the dehydration of monocarbonate. During thermal analysis, the monocarbonate present in the hydrate R3 mix experiences a two-step water loss. In the

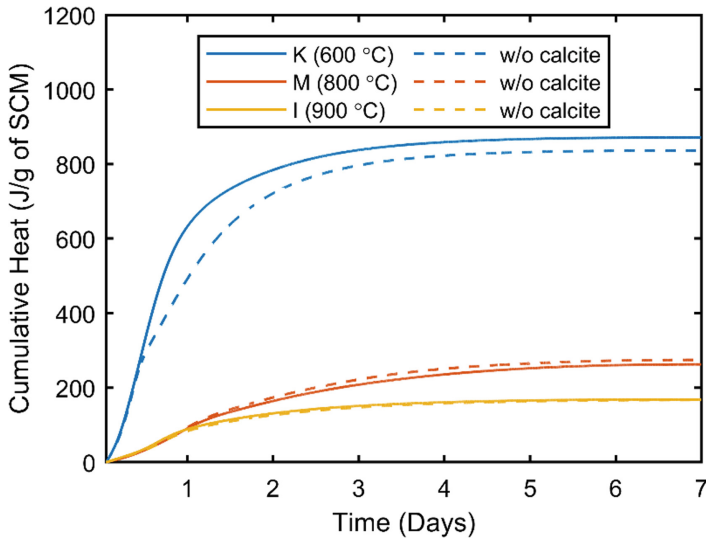


Fig. 1. Cumulative heat release for the pastes with and without calcite.

first step, five interlayer water molecules are lost between 60 and 200 °C, while the second step releases another six water molecules from its octahedral layers between 200 and 300 °C [17]. At around 350 °C, a peak can be observed in the metakaolin paste without calcite, which corresponds to the water loss from katoite [17]. As to the montmorillonite and illite hydrated pastes, the water loss from C-S-H phases is less significant compared to the metakaolin pastes. In addition, hydrotalcite usually has two water loss peaks, one at 270 and the other at 400 °C [17]. However, the water loss from hydrotalcite is negligible on the DTG curves, possibly due to its small quantity in these pastes.

3.3 Microscopy

As viewed under the fluorescence microscope, details related to the inherent porosity of the paste fragments are made visible through artifacts that arise from the two-stage fluorescent epoxy impregnation process (Fig. 4). Regions within the paste that represent the termini of the advancing fronts of fluid epoxy during the first stage of impregnation appear brighter than the surrounding regions of pure epoxy (e.g. brighter than the epoxy-filled pore spaces between quartz sand grains). These brighter regions arise due to internal reflection of fluoresced light along phase boundaries. In most cases, these internal reflections are subtle. For example, bright rings can be observed immediately around quartz sand grains at the epoxy interface. However, inside the paste fragments, these bright regions are even more evident, and especially so for the kaolin pastes (Figs. 4a and 4b). During impregnation, as fluid epoxy is forced by atmospheric pressure and capillary suction into the evacuated pore spaces inside the paste, the epoxy is also simultaneously going through polymerization reactions, and becoming more and more viscous, impeding its ability to further penetrate the pore structure. Eventually, as this front slows, the

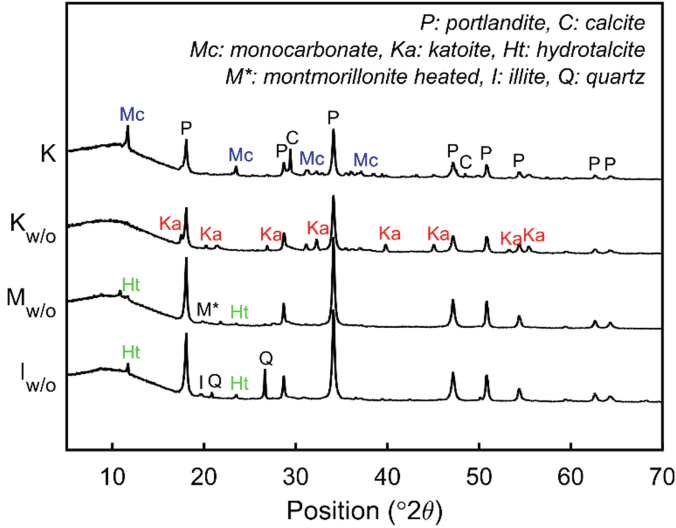


Fig. 2. XRD patterns for the hydrated pastes with and without calcite.

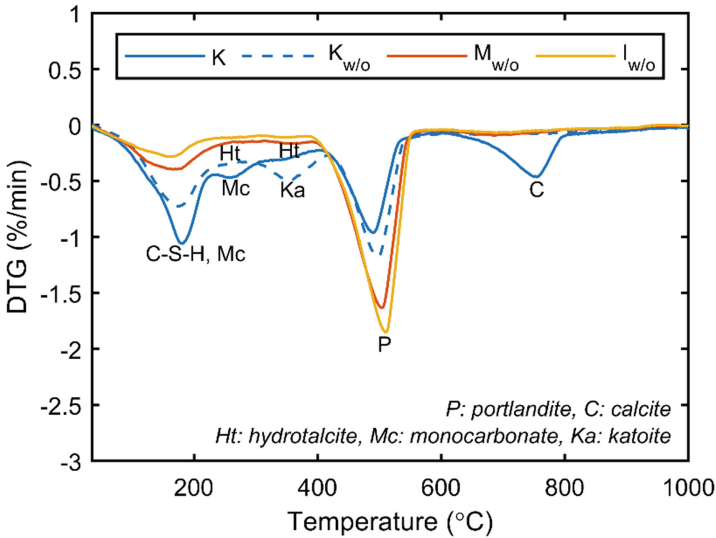


Fig. 3. DTG curves of the hydrated pastes with and without calcite.

epoxy is only able to wet the surfaces of pores, and no longer able to completely fill the pores. In these regions, after the epoxy sets, there exist small pockets of isolated empty pore space that are no longer interconnected (now blocked by hardened epoxy). It is along these boundaries that internal reflections occur, leading to their bright appearance.

During the second impregnation, performed after cutting and exposing the non-impregnated regions (beyond the initial penetration front), many of these leftover pockets

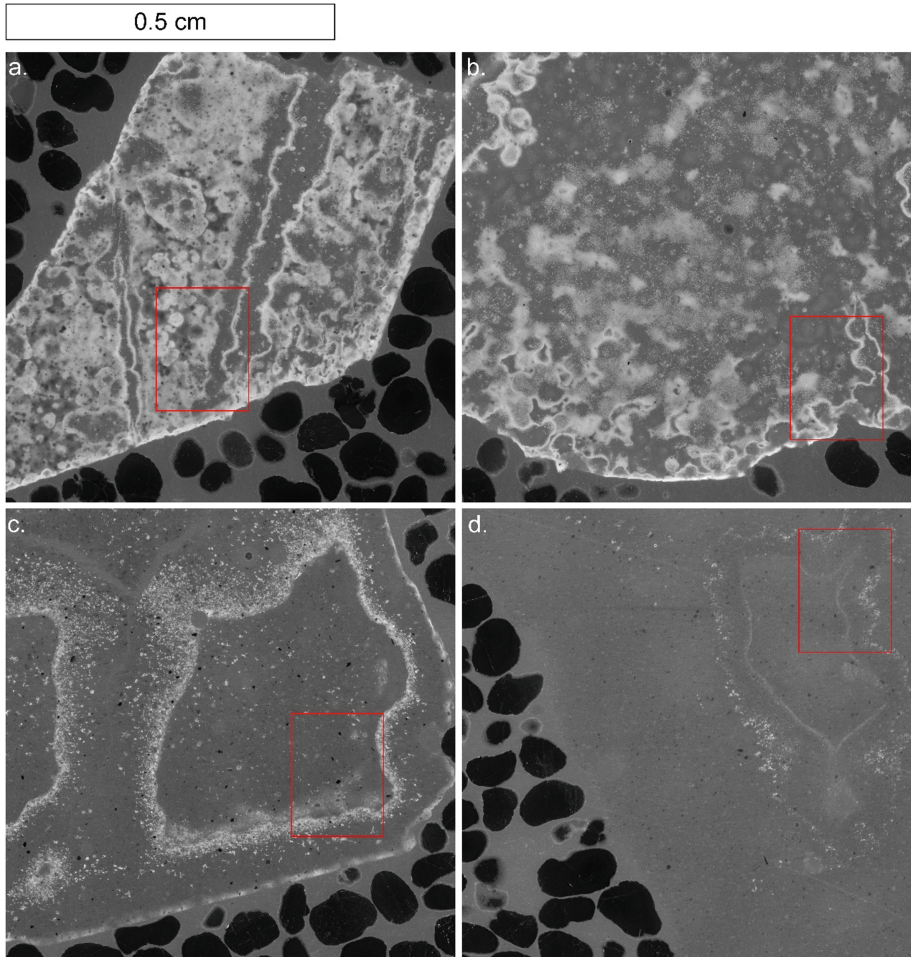


Fig. 4. Fluorescence images of paste thin sections with boxes drawn around areas of interest for elemental mapping: a). kaolinite paste with calcite; b). kaolinite paste without calcite; c). montmorillonite paste without calcite; and d). illite paste without calcite.

along the penetration frontal boundary remain inaccessible to the second wave of fluid epoxy. One of the unintended side effects of this incomplete epoxy impregnation is an inside view into how the formation of hydration products influences patterns of porosity. In the kaolinite pastes, where more intense hydration reactions occurred as compared to the montmorillonite and illite pastes, the porosity pathways are more tortuous and restricted, leading to more intricate patterns for the advancing front of epoxy. For the kaolinite pastes (both with and without calcite) the advancing epoxy front takes on complex balloon-shaped patterns, as revealed by the bright internal reflection artifacts (Figs. 4a and 4b). For the less hydration-reaction-intensive montmorillonite and illite pastes, the advancing front of epoxy is more linear, and the pore structure more uniformly filled behind the advancing front (Figs. 4c and 4d).

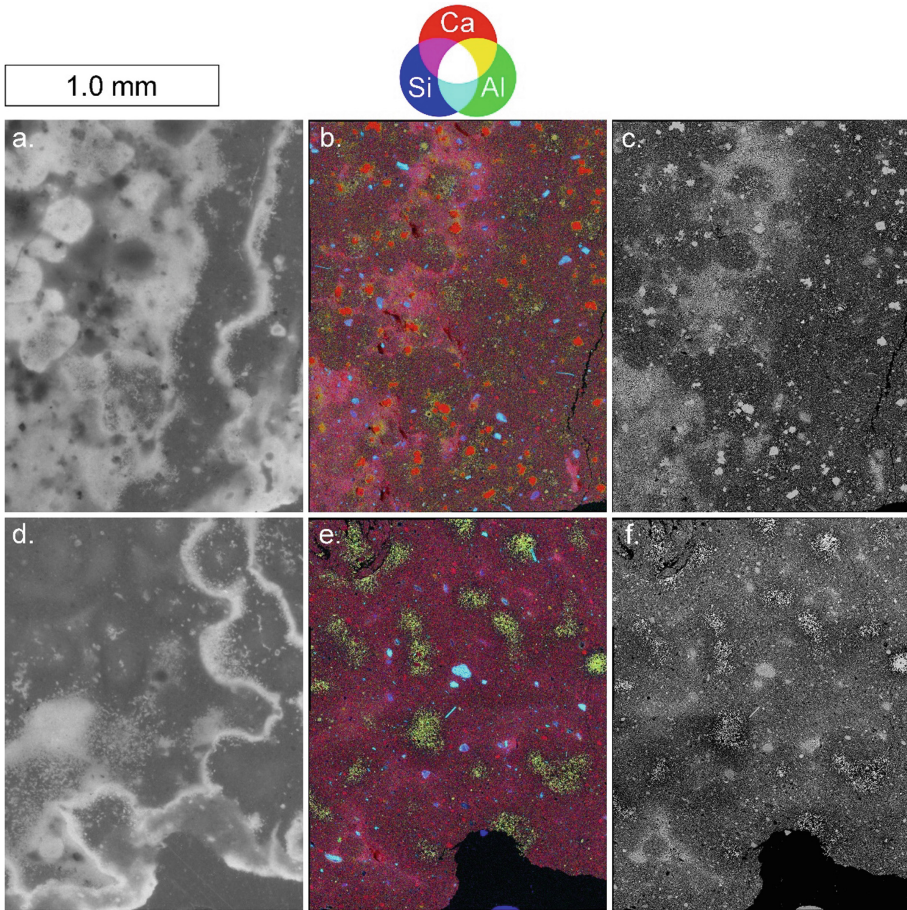


Fig. 5. Fluorescent (a), Ca-Si-Al false color (b), and BSE (c) images for kaolinite paste with calcite, and the same corresponding images for kaolinite paste without calcite (d, e, f).

In Fig. 4, areas outlined in red were more closely examined with the SEM (Figs. 5 and 6). In the characteristic $K\alpha$ X-ray elemental image for the kaolinite paste with calcite, red Ca-rich spots correspond to calcite particles (Fig. 5b). In the corresponding image for the kaolinite paste without calcite, these red spots are necessarily absent (Fig. 5e). The light yellow-green areas (rich in Ca and Al) in Fig. 5b may correspond to monocarbonate phases, as they tend to form in rings around the perimeters of calcite particles. In paste without calcite, the same clustered yellow green patches are also present, but these exhibit a relatively brighter yellow color (Fig. 5e) and likely correspond to the katoite phase observed in XRD. In the BSE images from both kaolin pastes (Figs. 5c and 5f) bright cloudlike features seem to correspond with magenta colored regions (rich in Ca and Si) in the elemental images and likely represent denser regions of C-S-H. Curiously, these

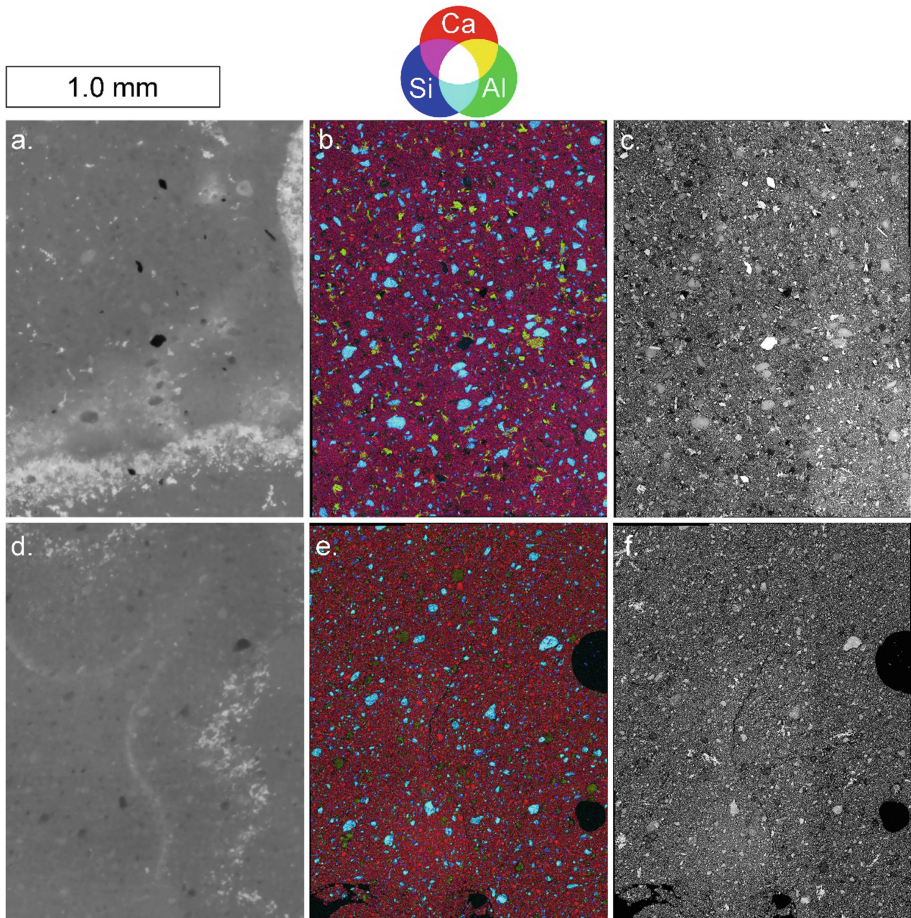


Fig. 6. Fluorescent (a), Ca-Si-Al false color (b), and BSE (c) images for montmorillonite paste, and the same corresponding images for illite paste (d, e, f).

C-S-H “clouds” appear related, in some instances, to the bright patterns from internally-reflected fluorescence (Figs. 5a and 5b), suggesting the presence or absence of C-S-H exerted some influence on the path of the fluid epoxy front.

For all the pastes, kaolinite, montmorillonite, and illite, remnant particles of calcined clay appear as bright turquoise spots (rich in Si and Al) in the characteristic $K\alpha$ X-ray elemental images. However, such particles are more abundant in the montmorillonite and illite pastes (Figs. 6b and 6e) suggesting their lower degree of participation in hydration reactions as compared to the kaolinite pastes. Ca and Al rich light green-yellow phases are also present in the characteristic $K\alpha$ X-ray elemental image from montmorillonite paste, but this time as distinct tabular crystals (Fig. 6b) that are possibly attributed to hydrogarnet. For the illite paste, not only were there remnant turquoise calcined clay particles rich in Si and Al, but also remnant calcined clay particles more depleted in

Si, appearing dark green in the characteristic $K\alpha$ X-ray elemental image. These Al rich particles also tended to be higher in Mg and Fe content.

4 Conclusions

According to the R3 test method calorimetry results, unsurprisingly, in order of increasing hydraulicity, was the illite paste, followed by the montmorillonite paste, then the plain kaolinite paste (without calcite), and finally, the most reactive, the kaolinite paste with calcite. As the degree of hydration increased, the interconnected pore paths became more complex, as evidenced by image artifacts left over from the advancing front from the first stage of fluorescent epoxy impregnation. Furthermore, as hydration increased, the frequency of remnant calcite clay particles decreased. And while more detailed quantitative EDS spot analyses work still needs to be done to better characterize the hydration phases, clear indications of the presence of monocarbonate, hydrogarnet, and C-S-H phases were found.

Acknowledgments. This research was funded by the NSERC Discovery Grants Program, RGPIN-2020-1509. Special thanks to Olga Perebatova, for her kind instruction as to all things R3.

References

1. Scrivener, K., Martirena, F., Bishnoi, S., Maity, S.: Calcined clay limestone cements (LC3). *Cem. Concr. Res.* **114**, 49–56 (2018)
2. Dhandapani, Y., Sakthivel, T., Santhanam, M., Gettu, R., Pillai, R.G.: Mechanical properties and durability performance of concretes with Limestone Calcined Clay Cement (LC3). *Cem. Concr. Res.* **107**, 136–151 (2018)
3. Sharma, M., Bishnoi, S., Martirena, F., Scrivener, K.: Limestone calcined clay cement and concrete: a state-of-the-art review. *Cem. Concr. Res.* **149**, 106564 (2021)
4. Avet, F., Scrivener, K.: Investigation of the calcined kaolinite content on the hydration of Limestone Calcined Clay Cement (LC3). *Cem. Concr. Res.* **107**, 124–135 (2018)
5. Antoni, M., Rossen, J., Martirena, F., Scrivener, K.: Cement substitution by a combination of metakaolin and limestone. *Cem. Concr. Res.* **42**(12), 1579–1589 (2012)
6. Lothenbach, B., Le Saout, G., Gallucci, E., Scrivener, K.: Influence of limestone on the hydration of Portland cements. *Cem. Concr. Res.* **38**(6), 848–860 (2008)
7. Avet, F., Snellings, R., Diaz, A.A., Haha, M.B., Scrivener, K.: Development of a new rapid, relevant and reliable (R3) test method to evaluate the pozzolanic reactivity of calcined kaolinitic clays. *Cem. Concr. Res.* **85**, 1–11 (2016)
8. ASTM C1897: Standard Test Methods for Measuring the Reactivity of Supplementary Cementitious Materials by Isothermal Calorimetry and Bound Water Measurements. ASTM International, West Conshohocken, PA (2020)
9. Londono-Zuluaga, D., et al.: Report of RILEM TC 267-TRM phase 3: validation of the R3 reactivity test across a wide range of materials. *Mater. Struct.* **55**(5), 142 (2022)
10. Fernandez, R., Martirena, F., Scrivener, K.L.: The origin of the pozzolanic activity of calcined clay minerals: a comparison between kaolinite, illite and montmorillonite. *Cem. Concr. Res.* **41**(1), 113–122 (2011)
11. Hollanders, S., Adriaens, R., Skibsted, J., Cizer, Ö., Elsen, J.: Pozzolanic reactivity of pure calcined clays. *Appl. Clay Sci.* **132**, 552–560 (2016)

12. He, C., Makovicky, E., Øsbæck, B.: Thermal stability and pozzolanic activity of calcined illite. *Appl. Clay Sci.* **9**(5), 337–354 (1995)
13. Cordoba, G., Irassar, E.F.: Sulfate performance of calcined illitic shales. *Constr. Build. Mater.* **291**, 123215 (2021)
14. He, C., Makovicky, E., Osbaeck, B.: Thermal treatment and pozzolanic activity of Na- and Ca-montmorillonite. *Appl. Clay Sci.* **10**(5), 351–368 (1996)
15. Snellings, R., Mertens, G., Elsen, J.: Supplementary cementitious materials. *Rev. Mineral. Geochem.* **74**(1), 211–278 (2012)
16. Song, H., Jeong, Y., Bae, S., Jun, Y., Yoon, S., Oh, J.E.: A study of thermal decomposition of phases in cementitious systems using HT-XRD and TG. *Constr. Build. Mater.* **169**, 648–661 (2018)
17. Scrivener, K., Snellings, R., Lothenbach, B. (eds.): *A Practical Guide to Microstructural Analysis of Cementitious Materials*, vol. 540. CRC Press, Boca Raton, FL, USA (2016)